Strongly Charged Polyelectrolyte Brushes: A Molecular Dynamics Study

Félix S. Csajka and Christian Seidel*

Max-Planck-Institut für Kolloid- und Grenzflächenforschung,† Am Mühlenberg, D-14476 Golm, Germany

Received January 25, 1999; Revised Manuscript Received December 29, 1999

ABSTRACT: We use molecular dynamics simulations to study polyelectrolytes end-grafted to a surface. Our model includes counterions explicitly and treats the full long-range Coulomb interaction. Strongly charged polyelectrolytes with no added salt are investigated, where the counterions are localized inside the brush and electroneutrality is satisfied locally. At this stage, we do not rule out that finite system size influences the prefactors of our scaling results. Irrespective of this question we find that the brushes are collapsed with a thickness linearly proportional to the chain length and the grafting density. The counterion distribution is strongly inhomogeneous, and counterion condensation can be observed although the Bjerrum length is smaller than the average bond length. The osmotic counterion pressure is much larger than the ideal gas value. Counterion diffusion is anisotropic and is enhanced at higher grafting densities. We compare our results to experiments and to scaling predictions.

I. Introduction

Polyelectrolytes have received a great deal of attention in recent years.[1,2] Polyelectrolyte brushes—charged polymers densely end-grafted to a surface—are important in several respects: They are a subject on which there is now a substantial body of theoretical work,[3−7] following the successful earlier work on uncharged brushes.[8−10] In recent years there have been several experiments on polyelectrolyte brushes, including polyelectrolytes end-grafted to a solid surface[11] and charged amphiphilic diblock copolymers in free-standing black films[12] or at the air/water interface.[13] Charged brushes are an efficient means for preventing colloids in polar media from flocculation.[14] This stabilization arises both from steric and electrostatic repulsion. In addition, a surface coated with polyelectrolytes is expected to be less sensitive to the salinity of the surrounding medium than a bare charged surface: a strongly charged brush is able to trap its own counterions and thus generates a layer of large effective ion strength.[4] It has been shown recently that polyelectrolyte brushes can be used in small devices such as pH-controlled gating in small porous filters.[15] It is also noteworthy that the water solubility of polyelectrolytes makes these applications environmentally friendly.

Both in experiment and in theoretical work, polyelectrolytes in solution are an interesting subject with many unresolved problems. In this situation, simulations are a promising tool to validate theoretical models and to probe quantities and regimes which are not easily observable experimentally. However, the simulation of polyelectrolytes remains challenging despite a strong effort in recent years.[17] First, long-chain molecules relax slowly, and the energy landscape of a dense polymer system is highly complex containing large regions of metastability. To obtain satisfactory statistics, one has to resort to long simulation times. Second, the correct treatment of the long-range Coulomb interaction in a periodic system requires special methods which are computationally expensive. This task is even more demanding in a brush geometry with planar periodicity (in the anchoring plane) and a finite slab perpendicular to the plane. Here, a straightforward application of Ewald sums is not possible.[18] Third, due to the long-range nature of the Coulomb interaction one has to pay special attention to effects caused by finite system size.

Following up on self-consistent work in ref 3, polyelectrolyte brush structure has been studied numerically by a combination of Monte Carlo and mean-field theory, using the Poisson−Boltzmann equation to handle electrostatic interactions.[19] Within the Debye−Hückel approximation, an enumeration study[20] and a Monte Carlo and self-consistent field approach were employed.[21] In ref 22, a Monte Carlo simulation of two interacting polyelectrolyte brushes was performed with a truncated Coulomb potential. In the present work, we avoid any mean-field treatment or truncation. Counterions are included explicitly, and we treat the full Coulomb interaction. We use a molecular dynamics technique which allows the investigation of an off-lattice polyelectrolyte in a parameter range which is comparable to experiments.

We adopt the freely jointed bead-chain model where each bead is coupled to a heat bath. This approach was introduced by Grest and Kremer to study polymers in solution.[23] Among other things, it has been used subsequently for uncharged polymer brushes[10] and for polyelectrolytes in solution.[24] In this model, polyelectrolytes are represented by flexible chains composed of charged monomers. The monomers are connected by nonlinear springs and end-grafted to a surface. The counterions are free charged particles, and there is no added salt in the system. The chains are fixed to the grafting surface by means of an uncharged endpoint monomer. The solvent is replaced by a dielectric background and a heat bath.

In the brush regime relevant to experiments, the effective polyelectrolyte concentration is very high, and the counterions are localized inside the brush. As a result, the counterion density to maintain a locally neutral system is very high. It is crucial to include the counterions explicitly to account for the ion osmotic

* To whom correspondence should be addressed.
† Mailing address: D-14424 Potsdam, Germany.

10.1021/ma990096l CCC: $19.00
Published on Web 03/16/2000

pressure in the brush: the balance between counterion osmotic pressure and the elastic restoring force of the end-grafted chains is assumed to govern the thickness of the brush layer in the so-called osmotic regime.[4] In addition, it has been shown numerically,[24−26] experimentally,[27] and in theoretical work[28] that counterion fluctuations in polyelectrolyte systems can modify the effective polyelectrolyte interactions qualitatively. Finally, it is instructive to study the counterions per se, i.e., how they give rise to local screening of the chains, how counterion condensation affects the system, and how they diffuse through the brush.

The paper is organized as follows. In section II we review the polyelectrolyte model and the simulation technique. The results on equilibrium properties of polyelectrolyte brushes are described in section III. Conclusions are given in section IV.

II. Model and Method

A. Simulation Model. We use stochastic molecular dynamics[23,29] to study the system in equilibrium. The equation of motion for particle i at position $\mathbf{r}_i(t)$ is the Langevin equation

$$m\frac{\mathrm{d}^2\mathbf{r}_i}{\mathrm{d}t^2} = -\nabla_i U - m\Gamma\frac{\mathrm{d}\mathbf{r}_i}{\mathrm{d}t} + \mathbf{W}_i(t) \tag{1}$$

where all particles carry the same mass m, and Γ is a friction constant which couples the particles to a heat bath. U is the potential energy defined in eq 3 below. The system is held at thermal equilibrium by a Gaussian random force $\mathbf{W}_i(t)$

$$\langle\mathbf{W}_i(t)\rangle = 0, \quad \langle\mathbf{W}_i(t)\cdot\mathbf{W}_j(t')\rangle = 6mk_\mathrm{B}T\Gamma\delta_{ij}\delta(t-t') \tag{2}$$

where the coupling to Γ is a consequence of the fluctuation−dissipation relation. The potential energy U of the system has four contributions, namely a Lennard-Jones term, a bonding potential, a repulsive wall potential and a Coulomb interaction:

$$U = U_\mathrm{LJ} + U_\mathrm{bond} + U_\mathrm{wall} + U_\mathrm{Coul} \tag{3}$$

The Lennard-Jones potential $U_\mathrm{LJ} = \sum_{i<j} u_\mathrm{LJ}(r_{ij})$ is a short-range potential acting between any particle pair ij with separation $r_{ij} = |\mathbf{r_i} - \mathbf{r_j}|$ smaller than a cutoff r_c

$$u_\mathrm{LJ}(r) = \begin{cases} 4\epsilon_\mathrm{LJ}\{(\sigma/r)^{12} - (\sigma/r)^6 + 1/4\} & \text{if } r < r_\mathrm{c} \\ 0, & \text{if } r \le r_\mathrm{c} \end{cases} \tag{4}$$

where the cutoff radius $r_\mathrm{c} = 2^{1/6}\sigma$ models a purely repulsive interaction between the monomers, as is appropriate for a polymer in a good solvent. We assume that monomers and counterions have the same Lennard-Jones diameter σ.

In addition to the Lennard-Jones potential, neighboring polymer segments i, j are coupled by a FENE (finite extensible nonlinear elastic) bond potential[16] $\sum'_{i<j} u_\mathrm{bond}(r_{ij})$, where the primed sum runs over all bonded monomers ij

$$u_\mathrm{bond}(r) = \begin{cases} -(kR_0^2/2)\log\{1 - r^2/R_0^2\} & \text{if } r < R_0 \\ \infty, & \text{if } r \ge \mathrm{R}_0 \end{cases} \tag{5}$$

with bond strength $k = 30\ \epsilon_\mathrm{LJ}/\sigma^2$ and maximum bond length $R_0 = 1.5\sigma$. This choice of parameters gives an average bond length of $b = 0.98\sigma$ which fluctuates by about 4%. The Coulomb repulsion between adjacent monomers slightly stretches the bond length compared to uncharged chains, where $b = 0.97\sigma$ has been reported.[10]

The polymer chains are anchored to the grafting surface by means of an uncharged end segment. The anchor segments are fixed and form a square lattice with lattice spacing $d = \rho_\mathrm{a}^{-1/2}$. All particles except the anchor segments interact repulsively with the surface at short distances $z_i < 0.5\sigma$, with z_i denoting the distance of particle i from the surface. For this purpose, we use $U_\mathrm{wall} = \sum_i u_\mathrm{wall}(z_i)$ with the shifted Lennard-Jones potential as defined in eq 4:

$$u_\mathrm{wall}(z) = u_\mathrm{LJ}(z+\Delta z), \quad \Delta z = (2^{1/6} - 0.5)\sigma \tag{6}$$

This choice is slightly different from the wall potential used in ref 10, but has similar features; i.e., both potentials are purely repulsive and vanish smoothly as $z \to 0.5\sigma$.

The implementation of the long-range Coulomb interaction requires special care. Our simulation box has periodic boundary conditions in two dimensions (x and y) and a finite extension in the z-direction. We use a technique proposed by Lekner[30] and modified by Sperb[31] to calculate the conditionally convergent Coulomb sum

$$U_\mathrm{Coul} = \frac{e^2}{4\pi\epsilon_0\epsilon}\sum_{n_z=-\infty}^{\infty}\sum_{n_y=-\infty}^{\infty}\sum_{i=1}^{N_\mathrm{tot}-1}\sum_{j=i+1}^{N_\mathrm{tot}}\frac{q_i q_j}{|\mathbf{r}_{ij} + n_x L\mathbf{e}_x + n_y L\mathbf{e}_y|} \tag{7}$$

where $\boldsymbol{e}_x$ and $\boldsymbol{e}_y$ are unit vectors in the x − and y -direction, respectively, and the indices n_x and n_y run over the periodic images of the simulation box. ϵ_0 and ϵ are the vacuum permittivity and the dielectric constant of the solvent, respectively, and q_i is the charge of particle i in units of the elementary charge e. N_tot is the total number of charges, and L is the planar box length. For the numerical treatment of eq 7, we refer the reader to the Appendix.

We assume that we have a system with matching ϵ boundary condition, so that no image charges appear across the anchoring surface. In experiments however the grafting substrate (or the air subphase) will generally have a lower dielectric constant than water. In this case, an estimate of the image charge energy has been given by Wittmer and Joanny.[32] For highly charged and densely grafted systems, the lateral charge density is approximately uniform and image charge effects are expected to be small.

B. Simulation Parameters. The temperature was set by $k_\mathrm{B}T = 1.2\epsilon_\mathrm{LJ}$, where ϵ_LJ is the Lennard-Jones energy unit. The Bjerrum length is given by $\lambda_\mathrm{B} = e^2/(4\pi\epsilon_0\epsilon k_\mathrm{B}T)$. It characterizes the length scale at which the electrostatic interaction is equal to the thermal energy $k_\mathrm{B}T$. The Bjerrum length of bulk water is 7.14 Å at room temperature, which sets the length scale for our simulation: we choose $\lambda_\mathrm{B} = 0.70\sigma$ so that σ is about 9.8 Å. Therefore the average bond length b is approximately 9.6 Å and the dimensionless Manning ratio is $\lambda_\mathrm{B}/b = 0.74$, slightly below the Manning condensation limit for a fully stretched chain.[2,33] Our model should be viewed as a coarse-grained representation of a flexible polyelectrolyte such as sodium polystyrenesulfonate (NaPSS) with a monomer length of 2.5 Å. Our charge separation b implies a fraction $f \approx 1/4$ of charged

monomers, similar to previous numerical work on polyelectrolyte solutions.[24] In comparison, Manning theory[33] predicts a charge fraction $f = 2.5$ Å/7.14 Å $= 0.35$ for a fully stretched PSS chain in water.

We have studied systems with $M = 36$ and $M = 9$ polyelectrolyte chains containing an uncharged anchor monomer and $N = 50$, 30, or 20 charged monomers per chain. Due to electroneutrality, there are $M \times N$ counterions. A simulation box of size $L \times L \times L_z$ was used, where $M/L^2 = \rho_a$ defines the grafting density and the system is periodic in the plane of the grafting surface. L_z was set to $(N + 10)\sigma$; in the course of the simulations, the counterions never visited the $z = L_z$ boundary of the simulation box.

Two types of finite size effects may interfere with the simulation results discussed below. First, the chain length N should be long enough to capture typical polymeric behavior. This has been verified by varying N from $N = 20$, $N = 30$, to $N = 50$. Several arguments presented below, such as the scaling behavior of the transverse density profiles $\rho_m(z)$ in a z/N master plot shown in Figure 6, justify the use of $N = 30$ chains. Second, due to possible self-interaction of the chains, a small lateral system size may also influence the large-scale properties such as brush thickness. To check this problem, we studied systems of $M = 9$ and $M = 36$ chains. A comparison of results for these two system sizes shows that the absolute values of large-scale properties (such as brush thickness) change. At this stage, we do not rule out that finite size effects will still influence the prefactor to our scaling results. However, the exponent of the scaling law of average brush height is unaffected. For the average endpoint height, the finite size influence is somewhat stronger. This is possibly related to the fact that, due to reduced charge density in the tail region, screening becomes weaker and any long-range effect is amplified. On the other hand, for small-scale properties such as counterion correlations the system size has no influence. To keep both effects small, we concentrate our discussion on the case of $M = 36$ chains of length $N = 30$. Note that these systems contain 2160 charged particles and simulations imply CPU times which require the use of parallel supercomputers.

The contour length of the polyelectrolytes corresponds to about 20−50 nm. A contour length of 20 nm is comparable to realizations of charged brushes at the air/water interface,[13] but 50 nm is roughly 3 times shorter than experiments on rigidly grafted polyelectrolytes.[11] The grafting densities studied range from $\rho_a\sigma^2 = 0.031$ to 0.141, corresponding to a surface area per polymer of 680−3100 Å.[2] These values are typical for experimental systems.[11−13] For lower grafting densities or shorter chains the end-to-end distance becomes comparable to the linear grafting distance $\rho_a^{-1/2}$. Very high anchoring densities have not been realized experimentally due to technical difficulties.[11,13]

The Gouy−Chapman length $\lambda_{GC} = (2\pi\lambda_B\Sigma)^{-1} = (2\pi\lambda_B N\rho_a)^{-1}$ is the length at which the counterions are effectively bound to a surface of charge density $e\Sigma = eN\rho_a$.[4] For a strongly charged polyelectrolyte brush, the Gouy−Chapman length is very small (between 0.27σ and 0.05σ for our systems), implying local charge neutrality for the brush. This point will be discussed in more detail in section III D.

Equation 1 was integrated using the velocity-Verlet algorithm.[29] A time step $\delta t = 0.007\tau_{LJ}$ and a friction constant $\Gamma = 0.5\tau_{LJ}^{-1}$ were chosen. It was verified that no drift in the total energy occurs under these conditions. For a Newtonian trajectory with the same time step, the total energy fluctuations are less than 10^{-4}. A rough estimate of the time scales accessed in our simulations is possible via the Lennard-Jones time unit $\tau_{LJ} = (m\sigma^2/\epsilon_{LJ})^{1/2}$. We assume that one chain segment corresponds to four chemical monomer units of PSS with a mass of 184 g/mol per monomer, yielding an order of magnitude estimate $\tau_{LJ} \approx 10$ ps. Our trajectories are roughly 10−100 ns long.

Table 1. Polyelectrolyte Brush Simulations[a]

N	M	$\rho_a\sigma^2$	T_{relax}	T_{run}	τ_m
50	9	0.094	1200	4200	83
50	9	0.0625	4129	4200	50
50	9	0.042	1858	4200	29
50	9	0.031	2060	4200	24
30	36	0.12	240	1680	46
30	36	0.094	430	1680	23
30	36	0.0625	500	1400	14
30	36	0.042	260	1340	11
30	9	0.094	3800	2800	46
30	9	0.0625	3360	2800	41
30	9	0.042	3977	2800	22
20	9	0.142	3080	2800	7
20	9	0.094	3080	2800	20
20	9	0.0625	3200	2800	22
20	9	0.042	3200	2800	42

[a] Monomer number N, number of chains M, grafting density ρ_a, relaxation time T_{relax}, length of equilibrium run T_{run}, and autocorrelation time τ_m for the brush thickness. On τ_m, the error is about 25%. Time unit is the Lennard-Jones time τ_{LJ}.

The molecular dynamics code was parallelized using a self-scheduling (master−slave) algorithm[34] for the force loop. Upon testing the parallel code for different processor numbers n, we found that the efficiency is optimal in the range of $n = 32$ to $n = 64$ processors, where an efficiency of over 90% is reached (the speedup for $n = 64$ processors is $0.94 \times 64 = 60$). Lower numbers of processors lead to a loss in efficiency due to the idle master processor, while large processor numbers are less efficient because communication time becomes a dominant contribution. It should be noted that the efficiency of the parallel code depends on the implementation of the Coulomb interaction; details of our force calculation are given in the Appendix.

III. Results and Discussion

The production runs are summarized in Table 1. The $N = 30$ and $N = 50$ simulations were performed on a Cray T3E−256 parallel computer. Figure 1 shows snapshots from the equilibrium trajectory for brushes of 36 chains of length 30 and grafting densities $\rho_a\sigma^2 = 0.042$, 0.0625, 0.094, and 0.12. In this figure, the connectivity of the chains has been preserved, such that the chains may extend beyond the simulation box. The counterions are assigned to the closest chain monomer.

In the following sections, errors were estimated by computing block averages[29] and by monitoring cumulative averages.[35]

A. Equilibration. Fully stretched chains with a line of counterions were used as initial configuration. The relaxation was monitored by studying the decay of the endpoint height of the chains. In addition, we looked for the convergence of cumulative averages for various observables (endpoint height, potential energy, and density profiles).

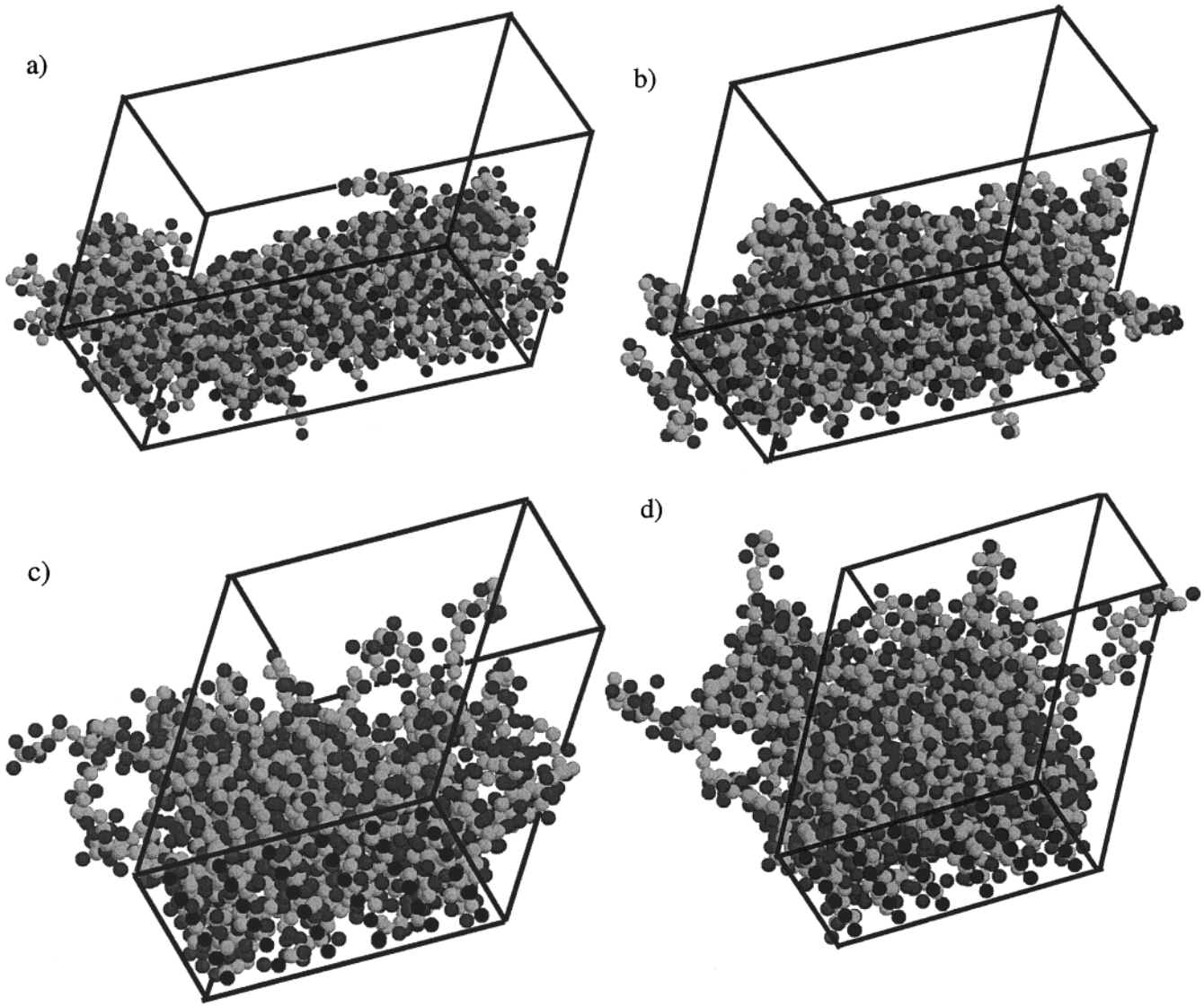

Figure 1. Polyelectrolyte brushes with $M = 36$ chains of length $N = 30$ at grafting density (a) $\rho_a\sigma^2 = 0.042$, (b) $\rho_a\sigma^2 = 0.0625$, (c) $\rho_a\sigma^2 = 0.094$, and (d) $\rho_a\sigma^2 = 0.12$. Counterions are assigned to the closest polyelectrolyte chain; polyelectrolyte chains are light gray, counterions are dark gray, and anchor monomers are black. The box height perpendicular to the grafting surface has been reduced for the sake of representation.

The equilibration times are presented in Table 1. As expected, longer chains take longer to relax to equilibrium; the relaxation times of brushes of length 50 are at least twice as long as that of their $N = 30$, 20 counterparts. Also, brushes with lower anchoring density relax more slowly than their denser counterparts. The systems with $M = 36$ chains were constructed by assembling four equilibrated systems of $M = 9$ chains. This procedure allows us to save equilibration time, since the assembled initial configuration is already close to equilibrium. The relaxation times T_{relax} for $M = 36$ systems are therefore much shorter (Table 1). Also note that the statistical uncertainty for $M = 36$ is lower than in systems of size $M = 9$ per data collection.

To estimate the statistical efficiency of the runs, we calculate the autocorrelation function $C_X(t)$:

$$C_X(t) = \frac{\langle \delta X(t)\, \delta X(0)\rangle}{\langle X^2\rangle - \langle X\rangle^2}, \quad \delta X(t) = X(t) - \langle X\rangle \qquad (8)$$

where X is the average endpoint height $\langle z_e\rangle$ or average brush thickness $\langle z_m\rangle$, defined in eq 9 below, with the notations $C_e(t)$ and $C_m(t)$, respectively. The autocorrelation function $C_e(t)$ of the endpoint height is shown in Figure 2. The decay of $C_e(t)$ is modulated by oscillations of the endpoint height. These modulations can also be observed in the perpendicular component of the counterion mean square displacement, section III F.

We extract a relaxation time from $C_m(t)$ using $\tau_m = \int_0^T C_m(t)\, dt/(1 - C_m(T))$.[10] The results are listed in Table 1. The inset of Figure 2 shows that the decay of $C_m(t)$ is approximately exponential at short times. The relaxation time generally increases for increasing chain length, although this trend is far less pronounced than for neutral chains in a good solvent.[10] For $N = 50$ and $N = 30$ chains, higher grafting densities lead to longer relaxation times, again in agreement with neutral chains. For chains of length 50 and 30, our relaxation times are consistent with the power law $\tau_m \propto \rho_a{}^{\lambda}$, $\lambda \approx 1$, observed for neutral brushes.[10] For $N = 20$ chains, the trend is reversed and the relaxation time actually increases for lower grafting density. This is possibly due to deviations from brushlike behavior for short grafted chains at lower grafting density.

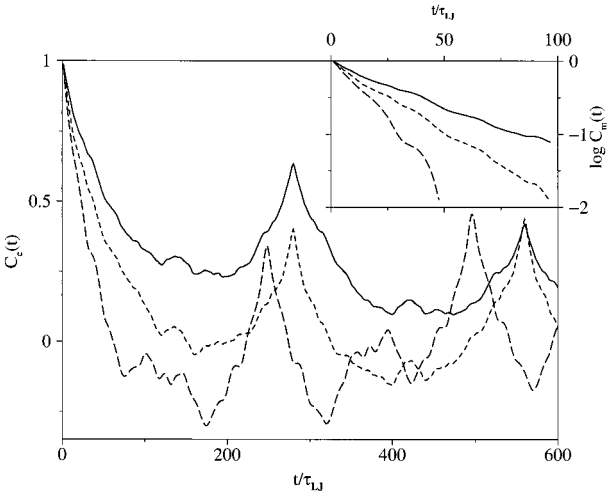

Figure 2. Autocorrelation function $C_e(t)$ of the endpoint height. Shown are chains of length 50 and grafting densities $\rho_a\sigma^2 = 0.094$ (solid line), $\rho_a\sigma^2 = 0.0625$ (dashed line), and $\rho_a\sigma^2 = 0.042$ (long-dashed line). Inset: Autocorrelation function $C_m(t)$ of the mean brush height on a semilogarithmic scale, same symbols as in main plot.

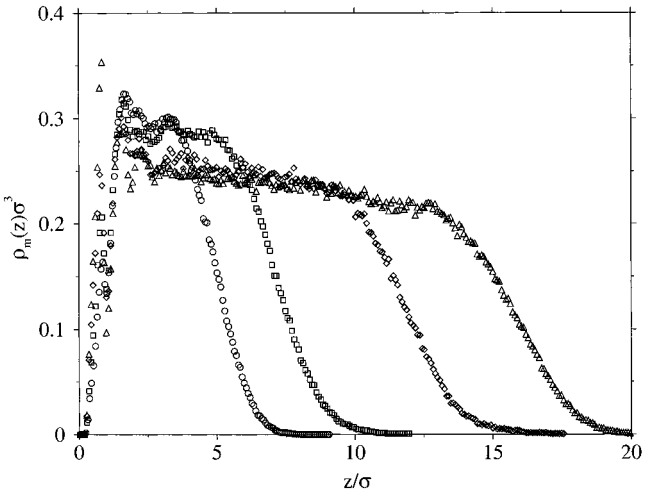

Figure 3. Density profiles of monomers $\rho_m(z)$, as a function of z, the distance from the grafting surface. Shown are profiles for brushes of 36 chains of length 30 at grafting densities $\rho_a\sigma^2 = 0.042$ (circles), $\rho_a\sigma^2 = 0.0625$ (squares), $\rho_a\sigma^2 = 0.094$ (diamonds), and $\rho_a\sigma^2 = 0.12$ (triangles). Errors are less than 5%.

B. Brush Profile and Height. Figure 3 gives the monomer density $\rho_m(z)$ as a function of the distance from the grafting surface. Shown are results for brushes with 36 chains of length 30. $\rho_m(z)$ is normalized such that $\int_0^\infty dz\ \rho_m(z) = N\rho_a$. The monomers show a short-range ordering close to the grafting surface, which becomes more pronounced at higher grafting densities. This is quite similar to uncharged brushes with only excluded-volume interactions. Note that the monomer density $\rho_m(z)$ is approximately constant at higher grafting densities. At lower ρ_a we observe a chain collapse similar to strongly charged chains in solution. Our results for $\rho_m(z)$ resemble polyelectrolyte brush profiles obtained by small-angle neutron scattering.[11]

The local net charge is shown in Figure 4, where we have assigned positive charges to counterions and negative charges to monomers, respectively. Charge neutrality is not only satisfied globally ($\int_0^\infty dz\ \langle\rho_{ci} - \rho_m\rangle = 0$), but also to a good approximation at the local level. The fluctuations at small z are a consequence of the

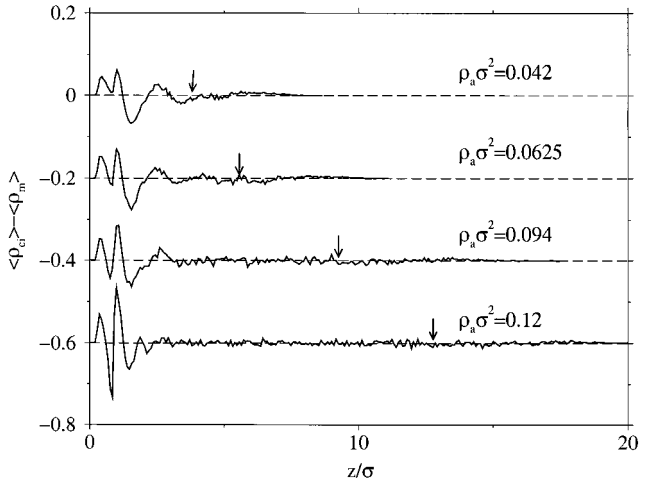

Figure 4. Local net brush charge $\langle\rho_{ci}\rangle - \langle\rho_m\rangle$ as a function of the distance from the grafting surface. Shown are systems of 36 chains of length 30, shifted by 0.2 unit for each grafting density. The average endpoint height $\langle z_e\rangle$ is indicated by an arrow. Monomers carry a negative, counterions a positive unit charge.

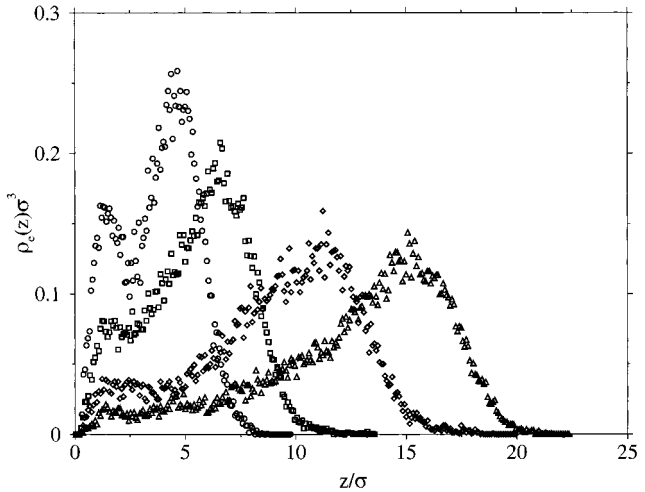

Figure 5. Endpoint distributions for systems of 36 chains of length $N = 30$. Grafting densities and symbols are the same as in Figure 3. Errors are less than 15%.

layering of the monomers close to the surface. At low grafting density, the Guoy−Chapman length is larger and a small tail of positive charge develops at the outer edge of the brush. Larger fluctuations at higher grafting densities are a consequence of the histogram construction because a constant binning interval was used for all grafting values.

Figure 5 gives the endpoint distribution $\rho_e(z)$ for length 30, normalized to unity. One notes that the endpoint distribution decays strongly inside the brush for high grafting density ($\rho_a\sigma^2 = 0.094$ and 0.12). At lower grafting density, a second peak of the endpoint distribution develops at small z, indicating that the chains are likely to fold back onto the surface. This is again reminiscent of the chain collapse of highly charged polyelectrolytes. Table 2 lists $\langle z_e\rangle$, the average endpoint distance from the grafting surface. Note that $\langle z_e\rangle$ is less reliable than $\langle z_m\rangle$ because of the reduced statistical significance and because of higher sensitivity to finite size effects.

The brush thickness is generally expected to be proportional to the chain length N, for both charged and neutral polymers. This feature is shown in Figure 6a

Table 2. Simulation Results[a]

N	M	$\rho_a\sigma^2$	$\langle z_m\rangle/\sigma$	$\langle z_{ci}\rangle/\sigma$	$\langle z_e\rangle/\sigma$
50	9	0.094	14.00 ± 0.1	14.30 ± 0.1	25.3 ± 0.3
50	9	0.0625	9.43 ± 0.08	9.63 ± 0.08	14.5 ± 0.2
50	9	0.042	6.22 ± 0.05	6.35 ± 0.05	8.8 ± 0.2
50	9	0.031	4.65 ± 0.05	4.73 ± 0.05	6.0 ± 0.2
30	36	0.12	7.85 ± 0.08	8.12 ± 0.08	12.8 ± 0.3
30	36	0.094	6.11 ± 0.08	6.32 ± 0.08	9.2 ± 0.3
30	36	0.0625	4.07 ± 0.05	4.21 ± 0.05	5.5 ± 0.2
30	36	0.042	3.03 ± 0.05	3.13 ± 0.05	3.8 ± 0.2
30	9	0.094	8.42 ± 0.08	8.72 ± 0.08	14.7 ± 0.3
30	9	0.0625	6.03 ± 0.05	6.24 ± 0.05	9.1 ± 0.2
30	9	0.042	4.31 ± 0.05	4.47 ± 0.05	5.7 ± 0.15
20	9	0.142	7.08 ± 0.08	7.46 ± 0.08	13.4 ± 0.2
20	9	0.094	5.75 ± 0.05	6.05 ± 0.05	10.0 ± 0.15
20	9	0.0625	4.39 ± 0.04	4.62 ± 0.04	6.7 ± 0.15
20	9	0.042	3.48 ± 0.04	3.68 ± 0.04	4.8 ± 0.15

[a] Average brush monomer height $\langle z_m\rangle$, average counterion height $\langle z_{ci}\rangle$, and average endpoint height $\langle z_e\rangle$.

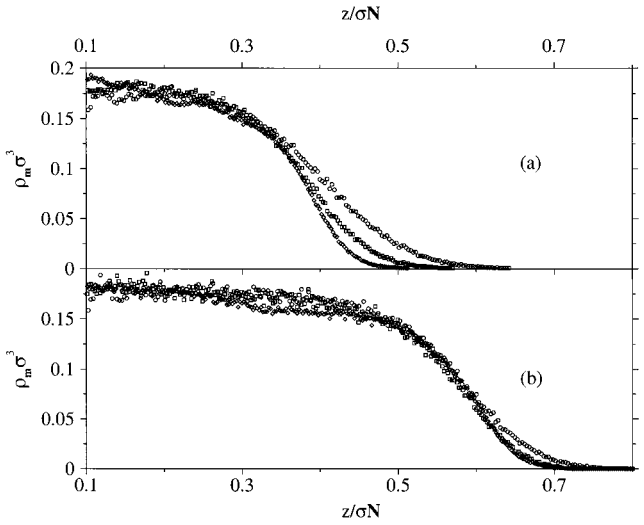

Figure 6. Monomer density profiles $\rho_m(z)$ versus rescaled distance z/N from the grafting surface for (a) grafting density $\rho_a\sigma^2 = 0.0625$ and $N = 20$ (circles), $N = 30$ (squares), and $N = 50$ (diamonds). (b) Same as (a), but for $\rho_a\sigma^2 = 0.094$. Oscillations close to the surface ($z/\sigma N < 0.1$) have been cut off.

for grafting density $\rho_a\sigma^2 = 0.0625$ by rescaling the coordinate z to z/N. The chains of length $N = 20$ clearly deviate from the rescaled N=50 profile. This effect becomes less pronounced as the grafting density decreases: in Figure 6b the same rescaling was done for grafting density $\rho_a\sigma^2 = 0.094$. Here the agreement between $N = 50$ and $N = 30$ is fairly good, but the $N = 20$ polyelectrolytes show a clear finite-size effect at the tail of the profile.

The average thickness of the brush and of the counterion layer was measured by taking the first moment of the density profiles

$$\langle z_m\rangle = \frac{\int_0^\infty z\rho_m(z)\,dz}{\int_0^\infty \rho_m(z)\,dz}, \quad \langle z_m\rangle = \frac{\int_0^\infty z\rho_{ci}(z)\,dz}{\int_0^\infty \rho_{ci}(z)\,dz} \qquad (9)$$

The average monomer and counterion heights for systems of $M = 9$ chains are shown in Figure 7a and Table 2. In Figure 7b and Table 2 we compare the scaling behavior of systems of $M = 9$ and $M = 36$ chains of length $N = 30$. While the prefactor changes somewhat compared to the small systems, we still find a scaling law $\langle z\rangle \propto \rho_a$ at higher grafting densities. This result is consistent with a constant particle density inside the brush layer, resulting from a close packing of the charged particles (monomers and counterions). From Figure 3 one can see that this regime is reached at higher anchoring densities. Although uncertainties related to finite system size cannot be entirely eliminated at this stage, i.e., possibly they still influence the prefactor to our scaling laws, the main result stays valid: The brushes are collapsed with a thickness linearly proportional to grafting density. For length 20 at high grafting, the chains are overstretched and the relation $\langle z\rangle \propto \rho_a$ breaks down. Note that the difference $\langle z_{ci}\rangle - \langle z_m\rangle$ increases slightly for growing ρ_a. This likely to be a steric effect, since the Gouy−Chapman length associated with a charged surface actually decreases for increasing surface coverage.

Our findings disagree with the accepted scaling law for charged brushes in the osmotic regime, which predicts a thickness $\langle z\rangle \propto Nbf^{1/2}$, independent of the grafting density[4,5] (f is the fraction of charged monomers, which is equal to 1 in our simulations). This relation is based on a balance between the osmotic pressure of an ideal gas of counterions of concentration $c_m f$, $\pi_{os} = k_B T\, c_m f$, and the elasticity of a Gaussian chain, $\pi_{el} = k_B T\rho_a h/(Nb^2)$. We believe that the disagreement is caused by the assumption that the counterions inside the brush form an ideal gas, which is only reasonable in the absence of counterion condensation.[36] If one studies the counterion properties, one finds in fact a strongly inhomogeneous density distribution as a result of counterion condensation (see sections III D and III E below).

C. Chain Structure. The overall shape of a polymer can be described by the shape factor $r = \langle R^2\rangle/\langle R_G^2\rangle$, where $\langle R^2\rangle$ is the average square end-to-end distance and $\langle R_G^2\rangle$ is the average radius of gyration squared. For a free Gaussian chain, one finds $r = 6$, and a rigid rod has the shape factor $r = 12$. As a measure for chain stretching, we compare our results in Figure 8 to end-grafted neutral chains, where we obtain the shape factor r=6.94 for an isolated chain. The ratio r is very sensitive to the grafting density of the brush. At high grafting densities, values typical of stretched chains are obtained. Similar values have been observed for dilute polyelectrolyte solutions.[24] At low grafting, the polyelectrolytes collapse and actually reach ratios below the value of a neutral chain in the mushroom state. In fact, it has been observed that polyelectrolyte brushes at low anchoring densities are more compact than uncharged brushes.[37]

For the intrachain structure of the grafted polyelectrolytes at all length scales, we examine the spherically averaged single chain structure factor

$$S(q) = \left\langle \left\langle \frac{1}{N+1}\left| \sum_{j=0}^{N} \exp(i\mathbf{q}\cdot\mathbf{r}_j)\right|^2 \right\rangle_{|\mathbf{q}|} \right\rangle \qquad (10)$$

Additionally, both the structure factor in the transverse direction $S(q_z)$ and the in-plane averaged $S(q_{xy})$ are calculated. Within the region $2\pi/R_e \ll q \ll \pi/b$, in analogy to free chains, $S(q)$ is expected to obey the scaling relation $S(q) \propto q^{-1/\nu}$. ν is the exponent of the N dependence of the chain radius. Figure 9 gives the spherically averaged structure factor. Within the range of the anchoring densities studied in the simulations, we obtain Flory exponents between 0.50 and 0.75. Thus, as expected the chains become moderately stretched with increasing ρ_a, but still remain clearly coiled. For small grafting densities we obtain two particular fea-

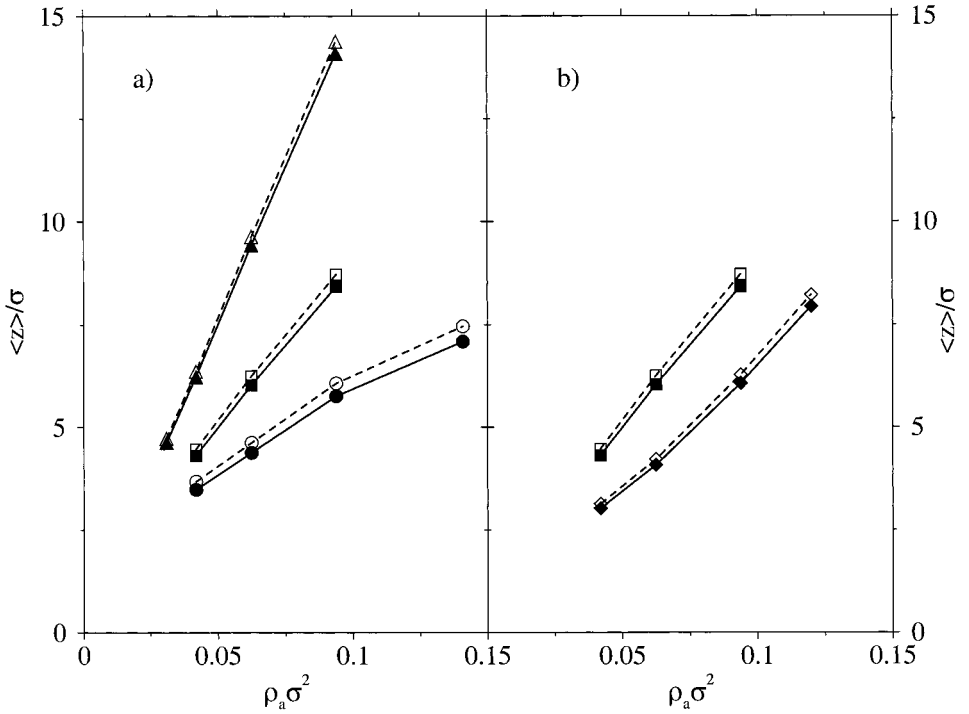

Figure 7. Average thickness of polyelectrolyte layer $\langle z_m \rangle$ (filled symbols) and average counterion height $\langle z_{ci} \rangle$ (empty symbols) for (a) $M = 9$ chains of length $N = 20$ (circles), 30 (squares), and 50 (triangles). (b) Same as (a), but for systems of length $N = 30$ and size $M = 36$ (diamonds) and $M = 9$ (squares). Error bars are smaller than symbol size (error estimates are given in Table 2).

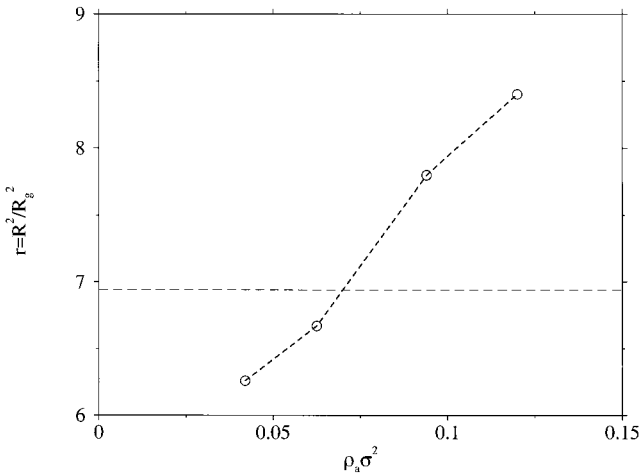

Figure 8. Shape factor $r = \langle R^2 \rangle / \langle R_G^2 \rangle$ for systems with $M = 36$ chains of length $N = 30$ as a function of grafting density. The horizontal dashed line gives the shape factor for an isolated end-grafted neutral chain. Error bars are less than 0.3 unit.

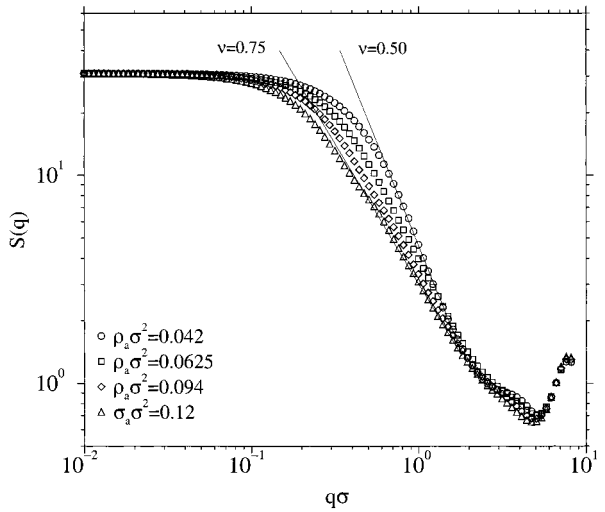

Figure 9. Spherically averaged structure factor $S(q)$ of systems with $M = 36$ chains of length $N = 30$ for different grafting densities ρ_a. The lines indicate scaling for $\nu = 0.5$ and 0.75.

tures: (i) The scaling exponent indicates a behavior below the good solvent limit where $\nu \approx 0.6$ is expected. (Note that 0.5 is the exponent for ideal chains.) (ii) At large q, corresponding to a distance of the order of two bond lengths, there appears an additional structure indicating a weak short-range order. Comparing with $S(q_{xy})$ and $S(q_z)$ shown in Figures10 and 11, respectively, one can see that this ordering is most clearly visible in the xy -plane. We believe that these features are due to counterion condensation (see section III D below) and to the high-density inside the polyelectrolyte layer (see Figure 3). Except at the smallest grafting density, all the in-plane averaged structure factors $S(q_{xy})$ show a quite similar scaling behavior close to the good solvent case. Obviously there is a crossover between two regimes at small and large q, respectively. Unfortunately our data do not reliably allow extraction of the corresponding length scale. In agreement with the brush profiles discussed above, the differing behavior for $\rho_a = 0.042$ indicates that the brush regime is not yet reached at that grafting density. Figure 11 gives the structure factor perpendicular to the grafting surface $S(q_z)$. The small dips in the low-q regime agree well (to within 10%) with the average endpoint position $\langle z_e \rangle$ (indicated by arrows), with the exception of $\rho_a\sigma^2 = 0.042$, where no q_z^* can be identified. At the highest grafting density a second dip can be identified in analogy to the oscillations of $S(q_z)$ of a rigid rod. However, compared to a rigid rod oriented perpendicular to the grafting surface, the structure factor is still dominated by disorder and tilting effects.

D. Counterions. The balance between polymer elasticity and counterion osmotic pressure determines the

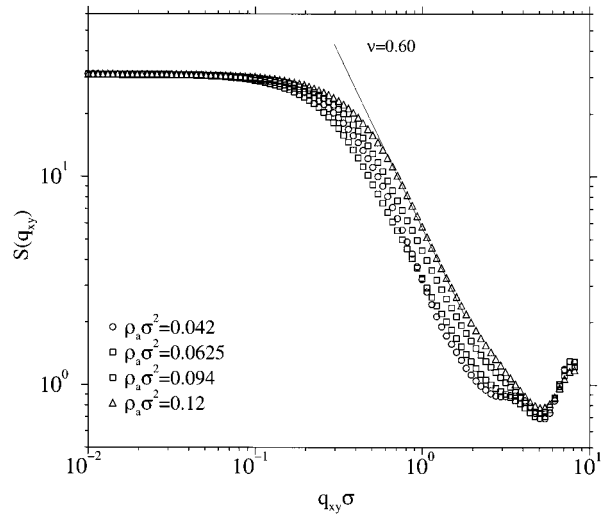

Figure 10. In-plane averaged structure factor $S(q_{xy})$ for the same systems as in Figure 9.

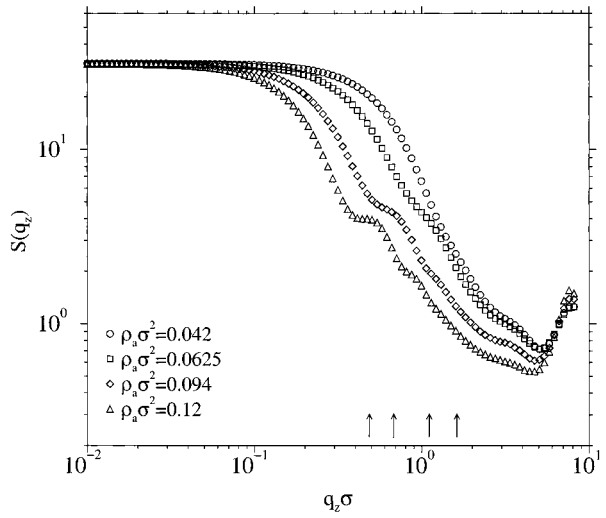

Figure 11. Structure factor $S(q_z)$ perpendicular to the grafting plane for the same systems as in Figure 9. Arrows indicate $q_z^* = 2\pi/\langle z_e \rangle$ for different grafting densities from $\rho_a\sigma^2 = 0.12$ (leftmost) to $\rho_a\sigma^2 = 0.042$ (rightmost).

overall structure of the brush in the osmotic regime. From the profile of the charge distribution $\langle \rho_{ci} - \rho_m \rangle$ (Figure 4) it is clear that the ions are indeed inside the brush, i.e., charge neutrality is satisfied locally. To estimate the amount of local screening and counterion condensation, we show the polyelectrolyte−ion pair distribution in Figure 12. The counterion distribution for the larger $N = 30$ systems does not differ significantly from the distributions for $N = 50$ shown in the figure. r is the separation between ion center and closest polyelectrolyte bond, and the distribution $p(r)$ is normalized according to $2\pi \int_0^\infty r\, dr\, p(r) = 1$. Assuming a step density profile for the counterions, the average ion density inside the brush can be estimated with $c_{ion}\sigma^3 = N\rho_a/2\langle z_{ci} \rangle \sigma^3$. For length 50 brushes, $c_{ion}\sigma^3 \cong 0.167$ regardless of grafting density. This estimate translates into a packing fraction of about 0.175 for monomers and counterions, using $\sigma/2$ as particle radius. While the average ion density is constant to a good approximation, the peak at $\sigma = 1$ depends on the grafting density, with the lowest $\rho_a\sigma^2 = 0.031$ showing the strongest increase. In a very rough manner, this trend can be explained by introducing an effective

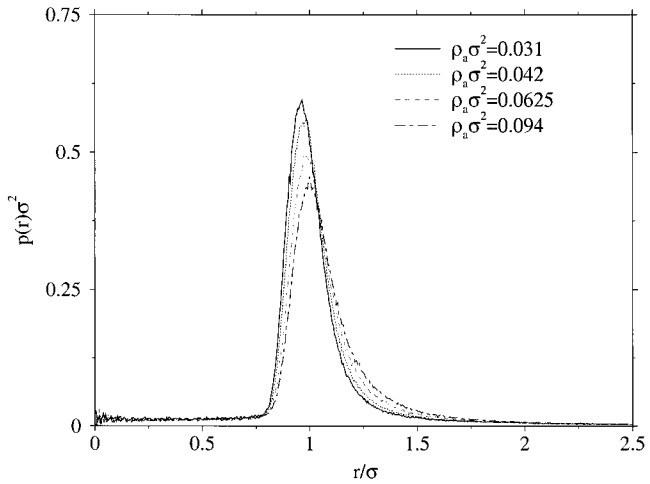

Figure 12. Ion−polyelectrolyte distribution function for chains of length 50. r is the separation between polyelectrolyte bond and counterion; error bars are approximately 5%.

Manning ratio $\xi_{eff} = N\lambda_B/2\langle z_m \rangle$, where we assume rigid rods in the z -direction with a rescaled line charge density $N/2\langle z_m \rangle$. In this rod model, the line charge increases as the brush layer contracts at smaller grafting density. This corresponds to our observation that counterion condensation occurs, and that the fraction of condensed counterions increases for lower grafting densities. Similar polyelectrolyte−counterion distributions have been calculated at lower bulk densities, but with added salt[38] or at much larger Bjerrum lengths.[39] At high polyelectrolyte concentration (comparable to local concentrations inside the brush layer) there is evidence for strong counterion condensation below the Manning threshold.[40]

The Debye screening length associated with the counterions is $\lambda_D = (1/4\ \pi\lambda_B c_{ion})^{1/2} \approx 0.83\sigma$, slightly smaller than the average bond length $b = 0.98\sigma$. This small length and the strong screening is a consequence of the high counterion concentration inside the brush.

A study of the partial ion energies suggests that the electrostatic ion−ion interactions are an important contribution. To visualize the ion−ion correlations along the polyelectrolyte, we define effective dipoles by adopting a method proposed in ref 39. Starting with the first chain monomer, we search for the closest counterion and assign a dipole vector **m** to that pair. We repeat the procedure for all the chain monomers, but exclude those counterions which have already been assigned. We study the correlations between dipole vectors by plotting the orientational order parameters $P_1 = \langle \cos\theta \rangle$ and $P_2 = (3\langle \cos^2\theta \rangle - 1)/2$ as a function of the separation r between dipole midpoints; $\theta = \arccos(\mathbf{e}\cdot\mathbf{e}')$ is the dipole−dipole angle between two unit dipoles with $\mathbf{e} = \mathbf{m}/|m|$. Figure 13 shows the orientational correlations between nearby dipoles. One finds that the correlation is strongest at a dipole separation of $r \approx 1\sigma$ and at small grafting density. Oscillations persist for larger separations up to around 3σ, consistent with local staggered ordering of the dipole vectors. Similar dipole orientations have be seen for polyelectrolytes at lower bulk density, but much larger Bjerrum length.[39]

To study the lifetimes of the effective dipoles, we monitor the mean square displacement $|\mathbf{m}(t) - \mathbf{m}(0)|^2$ as a function of simulation time. We find that the dipoles are short-lived due to counterion diffusion (see section III F below).

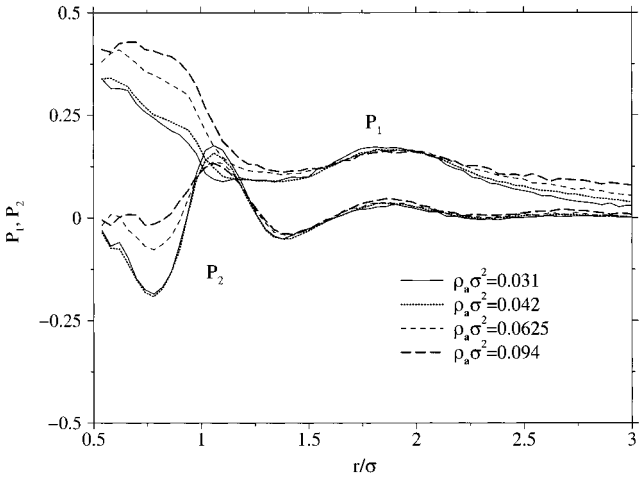

Figure 13. Orientational ordering of the effective dipole model for chains of length 50 (see text). Shown are $P_1 = \langle \cos \theta \rangle$ (upper set of curves) and $P_2 = (3\langle \cos^2 \theta \rangle - 1)/2$ (lower set of curves). Errors are about 5%.

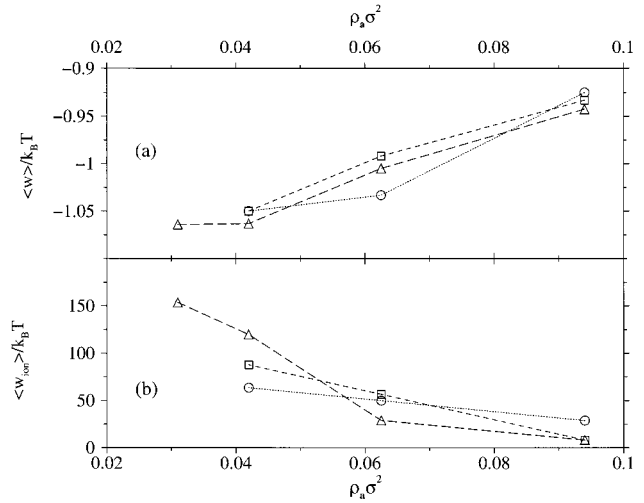

Figure 14. (a) Total pressure virial $\langle w \rangle$ per particle in units of k_BT. The ideal gas contribution is $+k_BT$. Error bars are about 0.05 k_BT. (b) Virial contribution per counterion to the osmotic pressure, arising from counterion−counterion repulsion. Error bars are about 5%. Results for chains of length 20 (circles), 30 (squares), and 50 (triangles).

E. Osmotic Pressure. The pressure of a homogeneous system of density c_{hom} is given by

$$\pi = c_{hom}\,(k_BT + \langle w \rangle) \tag{11}$$

$$\langle w \rangle = -1/(3N_{tot})\,(\sum_{i=1}^{N_{tot}-1} \sum_{j=i+1}^{N_{tot}} \langle \nabla U'_{ij} \cdot \mathbf{r}_{ij} \rangle + \langle U_{Coul} \rangle) \tag{12}$$

where the first term in eq 11 is the ideal gas contribution and the second term is the pressure virial[29] per particle. The virial in eq 12 is subdivided into contributions from the short-range part of the potential ($U' = U - U_{Coul}$) and the electrostatic part[41] to properly account for the long-range nature of the Coulomb interaction.[42] N_{tot} is the total number of particles, and $\nabla U'_{ij}$ is the short-range force on particle i due to j, along $\mathbf{r}_{ij} = \mathbf{r}_i - \mathbf{r}_j$.

The virial contribution to the pressure is given in Figure 14. We find that the virial compensates the ideal gas contribution k_BT almost exactly. This is just the statement of mechanical equilibrium in the brush layer: the ideal gas pressure balances the interaction contribution arising from the forces inside the brush.

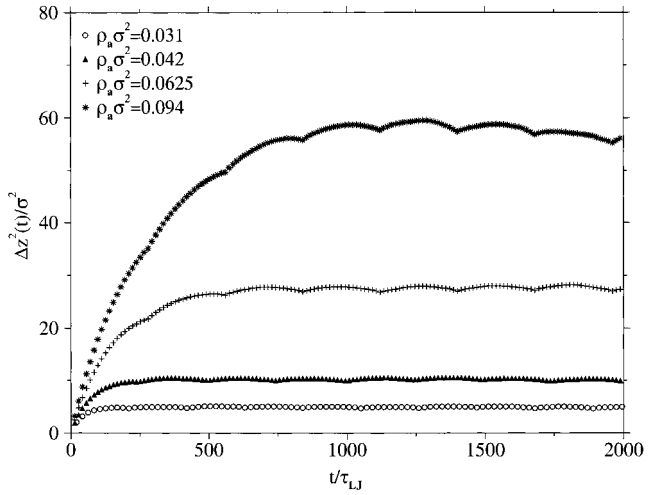

Figure 15. Counterion diffusion in brushes of chain length 50. MS displacement $\Delta z^2(t) = \langle [z(t) - z(0)]^2 \rangle$ perpendicular to the grafting surface.

The osmotic pressure of the counterions in the brush is given by two contributions: the ideal gas contribution of the ions confined to the brush layer, and the excess virial $\langle w_{ion} \rangle$ due to ion−ion repulsion. We calculate the excess virial by restricting the summation in eq 12 to counterions only. In Figure 14b we show

$$\langle w_{ion} \rangle = -1/(3N_{ci})\,(\sum_{i=1}^{N_{ci}-1} \sum_{j=i+1}^{N_{ci}} \langle \nabla U'_{ij} \cdot \mathbf{r}_{ij} \rangle + \langle U_{Coul} \rangle) \tag{13}$$

where N_{ci} is the total number of counterions. We find that the counterion interactions overwhelm the ideal gas pressure at all grafting densities. The small negative value of the total virial in Figure 14a arises from three large contributions which almost cancel one another: the repulsive chain−chain and counterion−counterion parts, and an attractive polyelectrolyte−counterion contribution.

This result for the osmotic pressure does not come unexpectedly in view of the strongly inhomogeneous counterion density, as seen in Figure 12 and by visual inspection of the brush (Figure 1). The contributions to the virial arise mainly from electrostatic interactions. In agreement with the polyelectrolyte−counterion distribution $p(r)$, the correlations are strongest at the lowest grafting density. These findings suggest that counterion condensation has to be included in a scaling approach to strongly charged brushes.[36]

F. Counterion Diffusion. The motion of the counterions can be traced with the mean square (MS) displacement $|\mathbf{R}(0) - \mathbf{R}(t)|^2$. For the brush geometry, it is appropriate to distinguish between lateral (x, y) and perpendicular (z) components. The motion of the counterions in the z-direction is bounded due to the anisotropy of the brush: it reaches a plateau which is roughly $(\langle z_{ci} \rangle/2)^2$ when the correlation with the initial z-value is lost. Figure 15 shows the perpendicular MS motion of counterions in brushes of length 50 and confirms that the long-time limit indeed approaches $(\langle z_{ci} \rangle/2)^2$ to within about 10%. The short- and long-time behavior of the perpendicular MS displacement can be described by

$$\langle |z(t) - z(0)|^2 \rangle = \begin{cases} 2D_z t & \text{for } t \ll \tau_P \\ (\langle z_{ci} \rangle/2)^2 & \text{for } t \gg \tau_P \end{cases} \qquad (14)$$

The plateau time τ_P gives the time scale for which the ions cross a distance of the order of the brush thickness. It is the crossover time between diffusive motion and constant MS displacement at long times and can be estimated with $\tau_P \approx \langle z_{ci} \rangle^2/8D_z$. The results for D_z, obtained from the initial slope of the perpendicular MS displacement, and the estimate for τ_P are collected in Table 3. At higher grafting density, the perpendicular diffusion constant increases, but the plateau time increases too due to the larger thickness of the brush. For $\rho_a\sigma^2 = 0.031$ it was impossible to extract a diffusion constant.

Assuming a constant brush thickness, the long-time perpendicular MS displacement is expected to be constant. However, an inspection of Figure 15 shows oscillations with a constant period τ_{osc}. A study of $C_e(t)$, the autocorrelation function of the endpoint height $\langle z_E \rangle$, reveals that the decay of $C_e(t)$ is modulated by oscillations with the same period seen in Figure 2. The time τ_{osc} represents the time scale for height fluctuations of the grafted polyelectrolytes to which the counterions are closely coupled.

At times larger than τ_P, the planar component $\mathbf{R}_{xy}$ dominates the diffusive motion of the counterions. We follow the planar MS displacement $\langle |\mathbf{R}_{xy}(t) - \mathbf{R}_{xy}(0)|^2 \rangle$ which is shown in Figure 16 for brushes of length 50. Ion diffusion is considerably enhanced for increasing grafting density; this is consistent with our results on counterion condensation, where we found that the fraction of free (uncondensed) counterions is larger at higher grafting density. At long times the planar MS displacement obeys

$$\langle |\mathbf{R}_{xy}(t) - \mathbf{R}_{xy}(0)|^2 \rangle = 4D_{xy}t, \quad t > \tau_{xy} \qquad (15)$$

where τ_{xy} is the time scale to reach diffusive motion. τ_{xy} decreases with increasing grafting density. We believe that the strong coupling between chains and counterions slows counterion motion at shorter times, when the chain dynamics dictates the planar displacement of the counterions. The planar diffusion constant D_{xy} is given in Table 3. Within the time frame of the production runs, the counterions diffuse on average over $2.3 \times L$, the lateral box length (for $\rho_a\sigma^2 = 0.031$), to $5 \times L$ (for $\rho_a\sigma^2 = 0.094$).

For free diffusive motion, a diffusion constant $D_{free} = k_BT/m\Gamma = 2.4\sigma^2/\tau_{LJ}$ is expected. The measured planar diffusion constants are 3−6 times lower, allowing a rough estimate of the fraction of condensed counterions: according to the lateral diffusion data, 64% (for $\rho_a\sigma^2 = 0.094$) to 84% (for $\rho_a\sigma^2 = 0.031$) of the counterions are condensed. For this estimate, we assumed that the diffusion for unbound counterions is given by D_{free}. A comparison of the perpendicular and planar diffusion constants shows that the perpendicular short-time diffusion is slower by a factor 4−5 for our simulation conditions. Possibly the small Gouy−Chapman length of the charged brush restrains the motion in the z-direction. Summarizing, the anisotropy of the system is also reflected in the motion of the counterions.

IV. Conclusion

In this work, strongly charged polyelectrolyte brushes are studied by molecular dynamics. We use a simple generic model which includes counterions explicitly and treats the full Coulomb potential. A Bjerrum length slightly below the Manning threshold is chosen, and a range of chain lengths and grafting densities comparable to experiments is investigated for strongly charged brushes with no added salt.

Table 3. Counterion Diffusion and Autocorrelation Times[a]

N	$\rho_a\sigma^2$	$D_{xy}/(\acute{o}^2/\tau_{LJ})$	$D_z/(\sigma^2/\tau_{LJ})$	τ_P/τ_{LJ}	τ_{osc}/τ_{LJ}
50	0.094	0.866 ± 0.02	0.174 ± 0.02	293	280 ± 2
50	0.0625	0.522 ± 0.02	0.146 ± 0.03	159	280 ± 2
50	0.042	0.457 ± 0.01	0.11 ± 0.04	92	249 ± 2
50	0.031	0.385 ± 0.01			181 ± 2

[a] D_{xy} and D_z are the counterion diffusion constants parallel and perpendicular to the grafting surface, respectively; τ_P is the plateau time, τ_{osc} is the period of the oscillation seen in Figure 15.

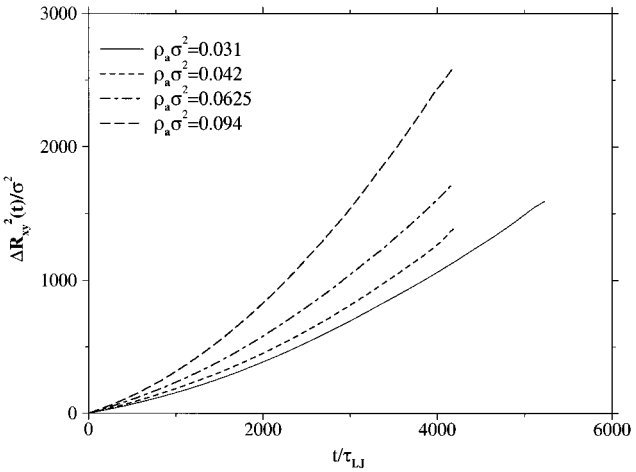

Figure 16. Counterion diffusion in brushes of chain length 50. MS displacement $\Delta R_{xy}^2(t) = \langle |\mathbf{R}_{xy}(t) - \mathbf{R}_{xy}(0)|^2 \rangle$ parallel to the grafting surface.

We find that the counterions are completely confined to the brush layer. In addition, strong correlations between polyelectrolyte chains and counterions result in a strongly inhomogeneous counterion distribution. The counterion osmotic pressure is much larger than the ideal gas value due to contributions from the force virial. Although the Bjerrum length is smaller than the average charge separation on the chain, strong counterion condensation is observed; the condensation peak increases for lower grafting densities. Similar behavior has recently been reported for polyelectrolyte solutions, where counterion condensation is seen to depend strongly on the density. At high density (comparable to the local density inside the brush layer) complete condensation is even reached while Manning theory predicts no condensed counterions.[40]

The chain structure of the grafted polyelectrolytes varies from strongly elongated and oriented at high grafting density to collapsed at low grafting. The brush thickness scales linearly with chain length N. The intrachain structure factor in the perpendicular direction shows the finite extension of the brush. The Flory exponents extracted from the spherically averaged structure factor range from $\nu = 0.50$ for low grafting density to 0.75 at high ρ_a.

In contrast to theoretical prediction for weakly charged polyelectrolytes, we find that the brush thickness scales linearly with grafting density ρ_a. Note that the same scaling is found for uncharged brushes in a poor solvent.[43] Recently it has been shown that the presence

of condensed counterions gives rise to an effective interaction which can change the solvent quality from good to poor.[44] The poor solventlike behavior is also visible in the chain structure at low grafting density. We therefore suggest the following interpretation for the scaling behavior of strongly charged polyelectrolyte brushes: (i) Due to the high charge density of the end-grafted polyelectrolytes, the counterions are localized inside the brush. (ii) High counterion density leads to counterion condensation even though the system is below the Manning threshold. (iii) The condensed counterions reduce the solvent quality from good to poor, which leads to the scaling behavior $h \propto \rho_a$ known for an uncharged brush in a poor solvent. Due to the long-range nature of the Coulomb interaction, large-scale properties, in particular the prefactors to scaling laws, are possibly still affected by finite system size. This problem will be adressed in more detail in future work. However, it should be pointed out that the main feature, obtained in this study, is unaffected: The brushes are collapsed with a thickness linearly proportional to grafting density.

The anisotropy of the system is also reflected in the counterion dynamics. The mean square displacement perpendicular to the grafting surface saturates at long times. The lateral diffusion increases for higher grafting density because the fraction of free (uncondensed) counterions becomes larger.

Acknowledgment. This work was supported by the Deutsche Forschungsgemeinschaft within the Schwerpunktprogramm Polyelektrolyte. We gratefully acknowledge a grant for the Cray-T3E at the John von Neumann-Institut for Computing in Jülich, Germany. We thank Stefan Förster, Jean-François Joanny, Roland Netz and René Sperb for useful discussions. Willi Erkens is acknowledged for his help in optimizing the parallel MD code.

Appendix: Coulomb Forces and Energy for a Finite Layer

This appendix gives the Coulomb forces and energy for a three-dimensional system with periodicity in two dimensions (2D). We use an approach due to Lekner[30] and Sperb.[31] An alternative method by Hautman and Klein[45] uses a 2D Ewald summation and expands for small $|z_i - z_j|/L$. This method only works well if the charges are confined to a thin layer in the z-direction. A comparison between the two methods can be found in ref 18.

The approach proposed by Lekner, which can also be applied to systems periodic in three dimensions, transforms the sum over all periodic images in the plane into a rapidly convergent expansion in terms of Bessel functions.

The x-component of the force on particle i due to j and its periodic images is

$$F_x = \frac{q_i q_j e^2}{4\pi\epsilon_0\epsilon L^2}\sum_{l=-\infty}^{\infty}\sum_{n=-\infty}^{\infty}\frac{\xi + l}{[(\xi + l)^2 + (\eta + n)^2 + \zeta^2]^{3/2}}$$
$$= \frac{q_i q_j \lambda_B k_B T}{L^2} 8\pi \sum_{k=1}^{\infty} k \sin(2\pi k\xi) \sum_{m=-\infty}^{\infty} K_0(2\pi k[(\eta + m)^2 + \zeta^2]^{1/2}) \quad \text{(A1)}$$

where we have used rescaled coordinates: $\xi = (x_i - x_j)/L$, $\eta = (y_i - y_j)/L$, and $\zeta = (z_i - z_j)/L$. $K_0(x)$ and $K_1(x)$ below are modified Bessel functions of the second kind.[46] The y-component of the force is obtained by exchanging ξ with η, as well as l with n. The z-component is

$$F_z = \frac{q_i q_j e^2}{4\pi\epsilon_0\epsilon L^2}\sum_{l=-\infty}^{\infty}\sum_{n=-\infty}^{\infty}\frac{\zeta}{[(\xi + l)^2 + (\eta + n)^2 + \zeta^2]^{3/2}}$$
$$= \frac{q_i q_j \lambda_B k_B T}{L^2}\left\{\frac{2\pi \sinh(2\pi\zeta)}{\cosh(2\pi\zeta) - \cos(2\pi\eta)} + 8\pi\zeta \times \sum_{k=1}^{\infty} k \cos(2\pi k\xi) \sum_{m=-\infty}^{\infty}\frac{K_1(2\pi k[(\eta + m)^2 + \zeta^2]^{1/2})}{[(\eta + m)^2 + \zeta^2]^{1/2}}\right\} \quad \text{(A2)}$$

Due to the anisotropy of the boundary conditions, the expression for the z-component of the force is different from that for the x- and y-components.

Both eqs A1 and A2 are rapidly convergent due to the asymptotic behavior of the Bessel functions

$$K_n(x) \to \sqrt{\frac{\pi}{2x}} \exp\{-x\}, \quad x \to \infty \quad \text{(A3)}$$

We truncate the Bessel sums for $x > 15$.

For small arguments of the Bessel functions, however, the convergence of the sums in eqs A1 and A2 is slow again. To overcome this drawback, we use Sperb's suggestion[31] to expand in terms of the Hurwitz zeta function $Z(s,a)$ defined by[46]

$$Z(s,a) = \sum_{k=0}^{\infty}{}' \frac{1}{(k + a)^s} \quad \text{(A4)}$$

where the term $k = -a$ is omitted in the primed sum.

Following Sperb[31] one obtains the identities

$$8\pi \sum_{k=1}^{\infty} k \sin(2\pi k\xi) K_0(2\pi k[(\eta + m)^2 + \zeta^2]^{1/2}) = \frac{\xi}{(\xi^2 + (\eta + m)^2 + \zeta^2)^{3/2}} + \sum_{k=0}^{\infty}\binom{-1/2}{k}((\eta + m)^2 + \zeta^2)^k\{Z(2k+2,1+\xi) - Z(2k+2,1-\xi)\} \quad \text{(A5)}$$

and

$$8\pi \sum_{k=1}^{\infty} \zeta k \cos(2\pi k\xi)\frac{K_1(2\pi k[(\eta + m)^2 + \zeta^2]^{1/2})}{[(\eta + m)^2 + \zeta^2]^{1/2}} = -\frac{2}{(\eta + m)^2 + \zeta^2} + \frac{1}{(\xi^2 + (\eta + m)^2 + \zeta^2)^{3/2}} + \sum_{k=0}^{\infty}\binom{-3/2}{k}((\eta + m)^2 + \zeta^2)^k\{Z(2k+3,1+\xi) - Z(2k+3,1-\xi)\} \quad \text{(A6)}$$

We use eqs A5 and A6 if the argument of the Bessel functions $K_0(x)$ and $K_1(x)$ respectively becomes smaller than $x = 0.15$. We have verified that the summations over k can be truncated after $k_{max} = 7$.

The Coulomb energy of a 2D periodically replicated ion pair can be obtained by integration of the force.[30,31]

$$U_{\mathrm{Coul}} = \frac{e^2}{4\pi\epsilon_0\epsilon L}\sum_{i<j} q_i q_j u_{\mathrm{Coul}}(r_{ij}/L)$$

$$u_{\mathrm{Coul}} = 4\sum_{l=1}^{\infty}\cos(2\pi l\xi)\sum_{m=-\infty}^{\infty} K_0(2\pi l[(\eta+m)^2+\zeta^2]^{1/2}) - \log[\cosh(2\pi\zeta)-\cos(2\pi\eta)] + C \quad \text{(A7)}$$

where the integration constant is given by $C = -1.603\,558\,9....$[30,31] Again, a representation in terms of the Hurwitz zeta functions is useful for small Bessel arguments:[31]

$$4\sum_{l=1}^{\infty}\cos(2\pi l\xi)K_0(2\pi l[(\eta+m)^2+\zeta^2]^{1/2}) = \sum_{k=1}^{\infty}\binom{-1/2}{k}((\eta+m)^2+\zeta^2)^k\{Z(2k+1,1+\xi)+Z(2k+1,1-\xi)\} - \Psi(1+\xi)-\Psi(1-\xi)+(\xi^2+(\eta+m)^2+\zeta^2)^{-1/2}+\log\{(\eta+m)^2+\zeta^2\} - 1.38629 \quad \text{(A8)}$$

In the last line, $\Psi(x)$ is the digamma function.[46]

References and Notes

(1) Förster, S.; Schmidt, M. *Adv. Polym. Sci.* **1995**, *120*, 51.
(2) Barrat, J.-L.; Joanny, J.-F. *Adv. Chem. Phys.* **1996**, *94*, 1.
(3) Miklavic, S. J.; Marcelja, S. *J. Phys. Chem.* **1988**, *92*, 6718. Misra, S.; Varanasi, S.; Varanasi, P. P. *Macromolecules* **1989**, *22*, 5173.
(4) Pincus, P. *Macromolecules* **1991**, *24*, 2912. Ross, R. S.; Pincus, P. *Macromolecules* **1992**, *25*, 2177.
(5) Borisov, O. V.; Birstein, T. M.; Zhulina, E. B. *J. Phys. II (Paris)* **1991**, *1*, 521. Zhulina, E. B.; Birstein T. M.; Borisov, O. V. *J. Phys. II (Paris)* **1992**, *2*, 63.
(6) Seidel, C. *Macromolecules* **1994**, *27*, 7085.
(7) Israels, R.; Leermakers, F. A. M.; Fleer, G. J.; Zhulina, E. B. *Macromolecules* **1994**, *27*, 3249. O. V. Borisov, E. B. Zhulina, E. B.; Birshtein, T. M. *Macromolecules* **1994**, *27*, 4795.
(8) Alexander, S. *J. Phys. (Paris)* **1977**, *38*, 983. de Gennes, P.-G. *Macromolecules* **1980**, *21*, 1069.
(9) Milner, S. T.; Witten, T. A.; Cates, M. E. *Europhys. Lett.* **1988**, *5*, 413. *Macromolecules* **1988**, *21*, 2610.
(10) Murat, M.; Grest, G. S. *Macromolecules* **1989**, *22*, 4054; *Phys. Rev. Lett.* **1989**, *63*, 1074.
(11) Mir, Y.; P. Auvroy, P.; Auvray, L. *Phys. Rev. Lett.* **1995**, *75*, 2863.
(12) Guenoun, P.; Schlachli, A.; Sentenac, D.; Mays, J. W.; Benattar, J. J. *Phys. Rev. Lett.* **1995**, *74*, 3628.
(13) Ahrens, H.; Förster, S.; Helm, C. A. *Macromolecules* **1997**, *30*, 8447; *Phys. Rev. Lett.* **1998**, *81*, 4172.
(14) Napper, D. H. *Polymeric Stabilization of Colloidal Dispersions*; Academic Press: New York, 1983.
(15) Park Y. S.; Ito, Y.; Imanishi, Y. *Chem. Mater.* **1997**, *9*, 2755.
(16) Binder, K., Ed.; *Monte Carlo and Molecular Dynamics Simulations in Polymer Science*; Oxford University Press: New York, 1995.
(17) Dünweg, B.; Stevens, M. J.; Kremer, K. In ref 16, pp 159−193 (Chapter 3.3).
(18) Tildesley, D. J. In *Computer Simulation in Chemical Physics*; Allen, M. P., Tildesley, D. J., Eds.; Kluwer Academic Publishers: Dordrecht, 1993, pp 23−47. Liem, S. Y.; Clarke, J. H. R. *Mol. Phys.* **1997**, *92*, 19.
(19) Granfeldt, M. K.; S. J. Miklavic, S. J.; Marcelja, S.; Woodward, C. E. *Macromolecules* **1990**, *23*, 4760.
(20) von Goeler, F.; Muthukumar, M. *Macromolecules* **1995**, *28*, 6608.
(21) Chen, H.; Zajac, R.; Chakrabarti, A. *J. Chem. Phys.* **1996**, *104*, 1579.
(22) Sjöström, L.; Åkesson, T.; Jönsson, B. *J. Chem. Phys.* **1993**, *99*, 4739.
(23) Grest, G. S.; Kremer, K. *Phys. Rev. A* **1986**, *33*, 3628.
(24) Stevens, M. J.; Kremer, K. *Macromolecules* **1993**, *26*, 4717; *Phys. Rev. Lett.* **1993**, *71*, 2228; *J. Chem. Phys.* **1995**, *103*, 1669.
(25) Stevens, M. J.; Kremer, K. *J. Phys. II (Paris)* **1996**, *6*, 1607.
(26) Grønbech-Jensen, N.; Mashl, R. J.; Bruinsma, R. F.; Gelbart, W. M. *Phys. Rev. Lett.* **1997**, *78*, 2477.
(27) Podgornik, R.; Parsegian, V. A. *Phys. Rev. Lett* **1998**, *80*, 1560.
(28) Ha, B.-Y.; Liu, A. J. *Phys. Rev. Lett.* **1997**, *79*, 1289; *Phys. Rev. Lett.* **1998**, *81*, 1011.
(29) Allen, M. P.; Tildesley, D. J. *Computer Simulation of Liquids*; Oxford University Press: Oxford, 1987.
(30) Lekner, J. *Physica A* **1991**, *176*, 524.
(31) Sperb, R. *Mol. Simul.* **1994**, *13*, 189; *Mol. Simul.* **1998**, *20*, 179.
(32) Wittmer, J.; Joanny, J.-F. *Macromolecules* **1993**, *26*, 2691.
(33) Manning, G. S. *J. Chem. Phys.* **1969**, *51*, 924.
(34) Gropp, W.; Lusk, E.; Skjellum, A. *Using MPI*; The MIT Press: Cambridge, MA, 1994.
(35) Chandler, D. *Introduction to Modern Statistical Mechanics*; Oxford University Press: New York, 1987.
(36) Csajka, F. S.; Netz, R. R.; Seidel, C. Preprint, 1999.
(37) Seidel, C.; van der Linden, C. C. Preprint, 1999.
(38) Stevens, M. J.; Plimpton, S. J. *Eur. Phys. J. B* **1998**, *2*, 341.
(39) Winkler, R. G.; Gold, M.; Reineker, P. *Phys. Rev. Lett.* **1998**, *80*, 3731.
(40) Holm, C.; Kremer, K. Preprint (to appear in Proceedings 50th Yamada Conference on Polyelectrolytes, Inuyama, Japan, 1998).
(41) Landau, L. D.; Lifshitz, E. M. *A Course of Theoretical Physics*, 3rd ed.; Pergamon Press: Oxford, UK, 1980; Vol. 5, p 94.
(42) Hummer, G.; Grønbech-Jensen, N.; Neumann, M. *J. Chem. Phys.* **1998**, *109*, 2791.
(43) Zhulina, E. B.; Borisov, O. V.; Pryamitsyn, V. A.; Birshtein, T. M. *Macromolecules* **1991**, *24*, 140. Murat, M.; Grest, G. S. *Macromolecules* **1993**, *26*, 3108.
(44) Brilliantov, N. V.; Kuznetsov, D. V.; Klein, R. *Phys. Rev. Lett.* **1998**, *81*, 1433. Schiessel, H.; Pincus, P. *Macromolecules* **1998** *31*, 7953.
(45) Hautman, J.; Klein, M. L. *Mol. Phys.* **1992**, *95*, 379.
(46) Abramowitz, M.; Stegun, I. A. *Handbook of Mathematical Functions*; Dover: New York, 1970.

MA990096L